Vertical Capacity Allocation in Inverter-Dominated Grids: Stability and Resilience Trade-Offs

Ailén Kreizer
Julius Frerk
Michael Popp
Markus Zdrallek
Institute of Power Systems Engineering
University of Wuppertal
Wuppertal, Germany
kreizer@uni-wuppertal.de

***Abstract*— As power systems transition toward inverter-based resources, the vertical distribution of generation and storage across voltage levels fundamentally reshapes grid dynamics. This paper quantifies how spatial capacity allocation affects frequency stability, voltage resilience, and fault propagation in low-inertia systems. Using dynamic RMS simulations on a large-scale multi-voltage network, we compare two architectures with identical total capacity: centralized generation at high voltage versus a more distributed allocation toward medium voltage. Three fault scenarios are evaluated under summer export and winter import conditions. Results reveal fundamental trade-offs: distributed layouts substantially reduce converter tripping during transmission faults, improve medium-voltage resilience, and accelerate recovery, while centralized layouts provide stronger high-voltage support but experience significantly higher disconnection rates. Frequency nadirs remain comparable, yet recovery dynamics diverge markedly due to differences in spatial damping and reactive power distribution. These findings demonstrate that stability margins depend critically on architectural decisions regarding capacity placement within the grid hierarchy.**

***Index Terms*-- Decentralized generation, Grid-forming inverters, Inverter-based resources, System stability, Voltage-level autonomy.**

I. Introduction

The ongoing transition from conventional synchronous generation toward inverter-based resources (IBRs) represents a key technical challenge of the energy transition. While generation was traditionally concentrated at extra-high-voltage (EHV) and high-voltage (HV) levels, increasing portions are now embedded within medium-voltage (MV) and low-voltage (LV) networks [1]. This vertical redistribution of generation can significantly change power exchange patterns, stability margins, and control coordination across voltage levels.

IBRs shift stability from mechanical to control-based phenomena, making their dynamic performance highly dependent on network strength and spatial aggregation [2]. Grid-forming (GFM) inverters enhance voltage and frequency stability compared to grid-following (GFL) designs, yet are sensitive to weak-grid conditions due to virtual impedance interactions [3]. Unlike synchronous machines (SM), IBRs react to disturbances within milliseconds through protection systems, creating susceptibility to cascading tripping, as observed in real incidents [4].

In parallel, new optimization approaches such as microgrid [5] and energy-cell concepts [6, 7] virtual power plants [8], and active distribution networks [9] promote local autonomy, resource aggregation, and bidirectional energy management as key strategies for future low-inertia systems.

Prior topology-centric work in single-layer transmission systems with synchronous dynamics, notably [10], identifies a structural trade-off: local redundancy favors resilience to cascading failures, whereas global redundancy favors frequency stability. At the distribution edge, [11] show that resilience varies with daily demand-photovoltaic (PV) cycles and that household batteries tuned for self-sufficiency yield limited system-level robustness. These studies highlight the importance of topology and autonomy objectives but do not address multi-voltage converter dynamics.

A systematic assessment of how the vertical allocation of generation and storage across voltage levels affects both global and local stability remains scarce. Much of the literature either optimizes spatial siting from an economic perspective [12] or focuses on single voltage levels for optimal placement of synthetic inertia [13]. Only a few recent studies compare architectural layouts [14], and even these are largely confined to frequency aspects.

This paper addresses this gap by comparing concentrated and distributed multi-voltage configurations with identical total capacities. Using a large-scale inverter-dominated test system, it quantifies how vertical allocation influences frequency and voltage stability, fault propagation, and resilience. Beyond analytical insights, the results offer practical guidance for capacity allocation and spatial planning in future low-inertia grids.

The paper is organized as follows. Section II introduces the test system and allocation variants. Section III describes the methodology, disturbance scenarios, and performance metrics. Section IV presents the results for the representative faults. Section V discusses the implications and key trade-offs. Section VI concludes and outlines future work.

II. Test System and Modeling Approach

A. Network structure

The analysis is performed on a synthetic large-scale multi-voltage network derived from the SimBench framework [15]. A 110 kV HV backbone is interfaced to the EHV grid through

979-8-3315-8138-1

three EHV/HV substations and feeds 15 MV areas via 15 HV/MV substations. The 15 MV areas span four archetypes; MV-connected wind exists in three of them, covering 12 of the 15 areas. Each MV area aggregates multiple LV feeders with residential and commercial loads, embedded PV generation (0.7 GW), and Battery Energy Storage System (BESS). The network includes over 3,000 IBR units (GFL or GFM). In the reference configuration, wind generation (2 GW) is allocated 85% to HV and 15% to MV levels, with only 24 MW SM representing a low-inertia system.

B. *Scenario Design and Operating Point Selection*

To systematically assess the impact of vertical capacity redistribution while maintaining network feasibility, a two-stage methodology was applied:

Stage 1: Annual time-series simulation (15-min) identified two critical operating points based on peak EHV power exchange:

- Summer scenario (Export): characterized by high PV and wind generation and reduced demand.
- Winter scenario (Import): low renewables, high demand, maximum HV import from the MV areas.

These boundary cases stress inter-level coupling under opposing power flow directions.

Stage 2: Capacity allocation and BESS integration

Two contrasting scenarios were defined by redistributing generation while keeping total capacity constant:

Variant C (Concentrated): Retains the baseline 85% HV/15% MV wind distribution.

Variant D (Distributed): shifts wind capacity toward MV (30% HV/70% MV) by up- and downscaling existing turbines, increasing MV self-sufficiency and reducing HV dependence. “Self-sufficiency” here refers to the operating points in which D achieves full local independence (Fig. 1).

BESS sizing follows a two-step approach. Initial capacity is proportional to installed PV capacity at 1.5 MWh per MW [16]. Additional BESS capacity is co-located with distributed wind sites to mitigate reverse power flows and enhance local voltage support. The resulting allocation for wind distributes 85% of BESS capacity to MV in D versus 80% at HV in C. BESS operation follows a revenue-oriented strategy: in summer, BESS charge to store surplus energy up to the revenue threshold, while in winter, BESS discharge to support grid demand. Fig. 1 summarizes the seasonal power exchange and transformer loading for both configurations.

All network data and controllers are identical; scenarios differ only in the vertical allocation of installed capacity across HV and MV levels, which changes inverter power ratings without modifying control, operating mode, or quantity.

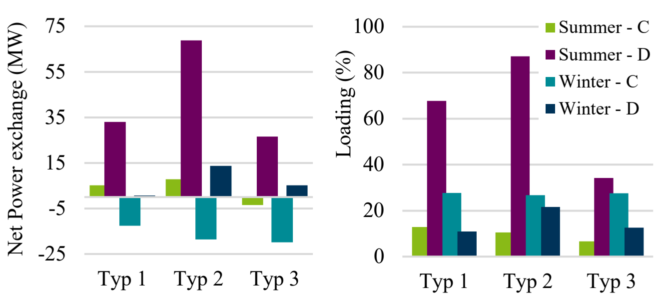

Figure 1. Net power exchange (left) and HV/MV transformer loading (right) for three MV area types under centralized (C) and distributed (D).

In summer (1.14 GW generation), BESS reach 100% State of Charge (SoC) from surplus generation. D increases transformer loading despite higher BESS, with type-2 transformers reaching 90% S_n versus 15–65% in others. In winter (0.41 GW), PV-BESS are depleted (0% SoC), wind-BESS at 30%. D achieves partial self-sufficiency and feeds back into HV, indicating greater local autonomy than C.

C. *Inverter modeling*

The IBRs are represented using generic dynamic templates derived from WECC models. Wind turbines and BESS are configured in GFM mode with droop-based active and reactive power control (1778 units), whereas PV (1562 units) systems employ GFL control schemes aligned with standard converter behavior. SMs (43 units) are described using IEEE conventional generator models. [17]

While the demand side follows the ENTSO-E [18] composite load model, incorporating both frequency and voltage dependency.

III. Methodology

A. *Setup and disturbances*

Dynamic RMS (Root Mean Square) simulations were performed in *DIgSILENT PowerFactory* [17] using an adaptive numerical integration step between 1 ms and 10 ms. All simulations were initialized from steady-state power flows with identical overall generation–load balances, ensuring that observed differences arise solely from the vertical distribution of generation and storage.

IBR protection uses instantaneous tripping at a voltage magnitude of 0.1 p.u., representing a simplified threshold-based model without time-dependent ride-through behavior. The applied threshold is loosely derived from the IEEE 1547 momentary cessation criterion [19] and allows converters to remain connected under deep but short voltage sags.

Three disturbances were considered: (1) a 100 MW HV generation trip; (2) a short-circuit at one of the three EHV–HV substations, cleared in 150 ms; (3) an MV short-circuit, cleared in 150 ms.

B. *Performance Metrics*

Frequency and voltage measurements are recorded at all HV and MV substations to assess spatial propagation and inter-level coupling. This multi-point monitoring enables consistent comparison of system resilience across progressively localized disturbances, from wide-area generation loss to distribution-level faults. Evaluated performance metrics include the frequency nadir (f_{min}) and zenith (f_{max}), Rate of Change of Frequency (RoCoF) over 0.5 s (Hz/s), the minimum voltage magnitude (V_{min}), and the recovery time (t_{rec}) of both voltage (V >0.9 p.u.) and frequency (|Δf| < 0.01 Hz) after the fault. The tripped generation share is defined as ($\Delta P_{trip} = \frac{P_{trip}}{P_{gen}^{pre}}$), where P_{gen}^{pre} is total active generation immediately before fault start.

C. *Normalization*

To enable multi-dimensional comparison, all performance indicators were normalized to a 0–10 scale: Score = 10 × (Value - Min)/(Max - Min). For metrics where lower values indicate better performance (e.g., tripping magnitude, recovery time), the scale was inverted.

979-8-3315-8138-1

IV. RESULTS

Three representative fault types were simulated to assess how vertical capacity redistribution influences frequency stability, voltage resilience, and converter coordination under realistic operating conditions. Each scenario exposes distinct trade-offs between centralized and distributed architectures.

Case 1: High Voltage Generator Outage

The sudden disconnection of a large HV generator induces an immediate active-power deficit and a small under-frequency event. At the HV level, the configuration D exhibits a slightly shallower frequency nadir and a smoother recovery compared with C (Fig. 2, left). In summer, the nadir improves from 49.986 Hz (C) to 49.99 Hz (D), while in winter the difference narrows to 4 mHz. Post-fault RoCoF is reduced by 20-46% in D, with greater improvement in winter scenarios (30-46%) compared to summer (19-39%), reflecting a slower but more damped resynchronization. Both variants exhibit well-damped recovery with negligible overshoot (<0.3 mHz). At the MV level, frequency deviations closely follow the HV profile in both variants, with differences below 5 mHz.

In general C retains a slightly stiffer voltage (V≈ 1.005 p.u.) while D stabilizes at ≈ 0.995 p.u., indicating that the redistribution of reactive power among multiple converters in D slightly lowers the local voltage but avoids transient peaks. Both systems remain well within the operational band (±2%), confirming that the event primarily excites frequency rather than voltage dynamics. The voltage response at a representative MV, e.g., MV8 (Fig. 2, right) shows that the outage only marginally affects voltage magnitudes.

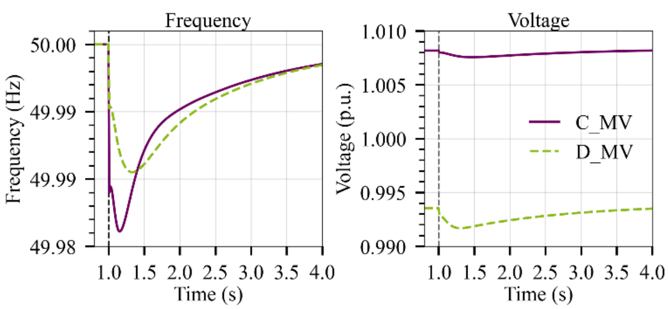

Figure 2. System frequency at HV (left) and voltage at MV8 (right) following the HV generator outage in summer.

Overall, the distributed layout shows stronger damping and a milder dynamic response in the studied scenarios: the frequency nadir improves, RoCoF decreases, and MV voltages settle without overshoot. The centralized setup reacts faster but with steeper gradients and slight voltage amplification. This indicates that vertical allocation improves the containment of HV-origin disturbances in the studied scenarios, converting a system-wide impulse into a short, well-damped transient.

Case 2: High Voltage Short-Circuit

A three-phase fault at an EHV/HV substation represents, in this study, the most severe transmission-level disturbance. The directly faulted transformer is excluded from evaluation. Both configurations show nearly identical frequency nadirs (~49.94 Hz), but voltage response differs markedly: C maintains higher V_{min} in summer (0.597 vs 0.477 p.u., +25%) and winter (0.417 vs 0.381 p.u., +8%), indicating stronger HV voltage support. This benefit, however, comes at the cost of resilience: summer tripping through voltage-based protection reaches 180 MW (15.9% generation) in C versus 43 MW (3.8%) in D, a 76% reduction. Winter shows the same 4:1 ratio (12 MW vs 3 MW), confirming that centralized configurations increase vulnerability to simultaneous disconnections despite better voltage retention at HV.

At the MV level, the disturbance propagates with inverse performance characteristics. Voltage nadirs range from 0.23–0.84 p.u. in C and 0.24–0.91 p.u. in D, with D providing better voltage retention in most areas (11/15), reflecting a higher availability of reactive power support at local level, whereas C relies on distant HV backfeed through congested transformers. Recovery dynamics confirm the advantage: D restores voltage above 0.9 p.u. within 0.22 s compared to 0.35 s in C, shortening critical undervoltage exposure by approximately 37%. Post-fault RoCoF drops from 0.162 to 0.016 Hz/s in summer and from 0.137 to 0.058 Hz/s in winter, reflecting a 65–90% mitigation and improved damping.

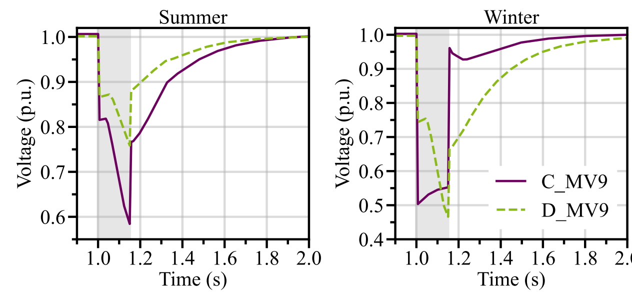

Figure 3. Voltage at MV9 during (grey) and after HV fault.

Area MV9, located electrically proximate to the faulted HV bus, exemplifies some trends (Figs. 3–4). As shown in Fig. 3, voltage collapses to 0.58 p.u. (C) versus 0.76 p.u. (D) under summer conditions, and to 0.50 p.u. (C) versus 0.47 p.u. (D) in winter. The temporary load relief during low voltage creates distinct frequency signatures (Fig. 4): C shows transient overfrequency (50.08 Hz summer, 50.04 Hz winter) due to power surplus, while D shows brief underfrequency (49.90 Hz summer, 49.84 Hz winter) as converter current limitation dominates the local balance. After clearance, D re-synchronizes ≈0.2 s earlier and recovers without oscillations or overshoot toward 1.0 p.u., while C displays sustained oscillations before settling.

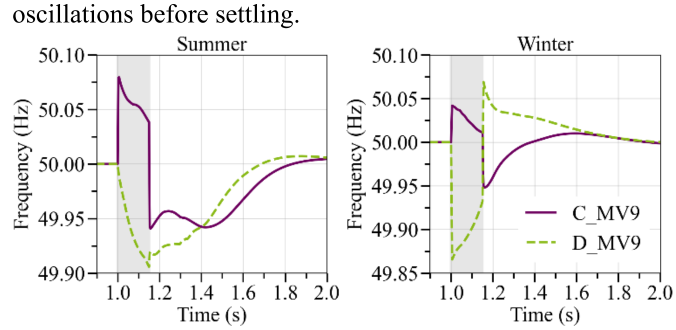

Figure 4. Frequency at MV9 during (grey) and after HV fault.

This case highlights a key design trade-off: C maximizes HV voltage support (8–22% higher nadirs) but sacrifices generation security and MV resilience. The 4:1 tripping ratio marks not only a quantitative but a qualitative shift in contingency severity: in C, a HV fault becomes a system-wide generation loss event; in D, it remains a localized voltage transient. With D's average 7% MV voltage improvement (range 5–15% across areas), 65–90% RoCoF reduction, and 37% faster recovery, the distributed layout achieves higher overall stability margins despite accepting 8–22% lower HV voltage nadirs. Spatial distribution adds defensive depth: faults no longer cascade through protective disconnections, resulting in more localized and shorter post-fault transients in the analyzed scenarios.

Case 3: Medium-Voltage Short Circuit

A three-phase fault in MV4 (representative example) evaluates disturbance propagation from a local fault on the distribution level. The event is largely confined to the affected MV area: across HV and the 14 unaffected MV areas, frequency deviations remain below 0.01 Hz with post-fault nadirs averaging 49.993 Hz, and voltage deviations at HV stay minor ($\Delta V_{min} \approx 0.01$ p.u.).

On the affected area during the fault, active power rises in all configurations due to transient converter current injection (Fig. 5). The effect is stronger in D, where MV-GFM units react almost instantaneously, reaching summer peaks above 100 MW versus C's smaller rise. Converter tripping occurs during the fault: 5.3 MW (summer) and 8.9 MW (winter) in D, versus 2.4 MW and 6.2 MW in C. The relative impact differs significantly, only 0.47% of capacity in summer but 2.17% in winter (4.6× times larger). This lower headroom explains the stronger seasonal variation in post-fault behavior.

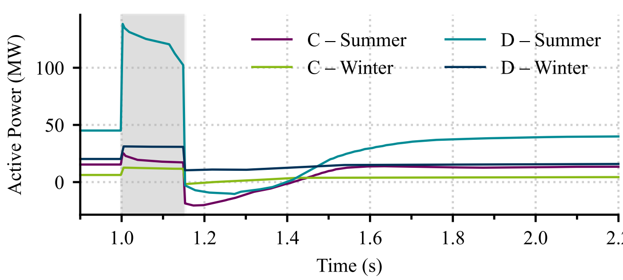

Figure 5. Active Power reaction of generation in MV4

This disconnection explains the frequency drop in MV4 after clearing (Fig. 6): available generation is lower while loads re-accelerate. In winter, D's coordinated BESS reversal delivers a short, well-damped support pulse (≈ 200 ms), achieving RoCoF = 0.46 Hz/s versus 4.88 Hz/s in C (–90%). In summer, D shows 5.73 Hz/s versus 2.60 Hz/s in C. Despite higher local RoCoF in summer-D, overall performance remains superior: D recovers 0.18–0.25 s faster (35–42%), with MV4 voltage returning to 0.9 p.u. within 0.4 s versus 0.6–0.65 s in C. During the fault, frequency at MV4 is invalid because voltage collapse prevents phase tracking; post-clear metrics are computed onward.

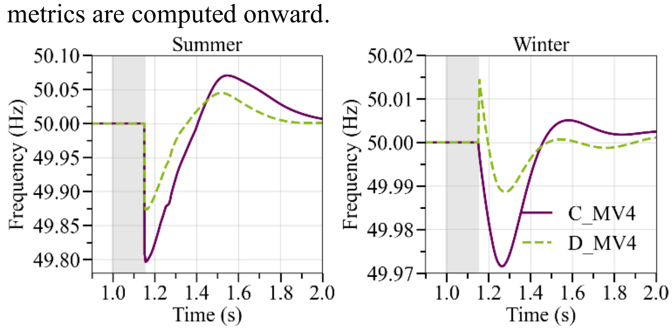

Figure 6. Frequency at MV4 during (grey) and after MV fault.

Fault impact remains spatially confined in both configurations. Fig. 7 shows frequency in neighboring MV9: despite proximity to the faulted area, deviations between C and D remain below ±0.01 Hz. In summer, C's load-relief produces brief overfrequency (+0.02 Hz), while D's current limitation yields small underfrequency (–0.03 Hz); in winter, both converge near nominal but D settles faster. Across all unaffected areas, voltage deviations stay within ±0.05 p.u. and frequency within ±0.01 Hz.

The distributed configuration turns a severe local fault into a confined transient with clear benefits: 30–42% faster voltage recovery, high spatial containment (< 0.01 Hz neighbor deviation), and 90% RoCoF reduction in winter.

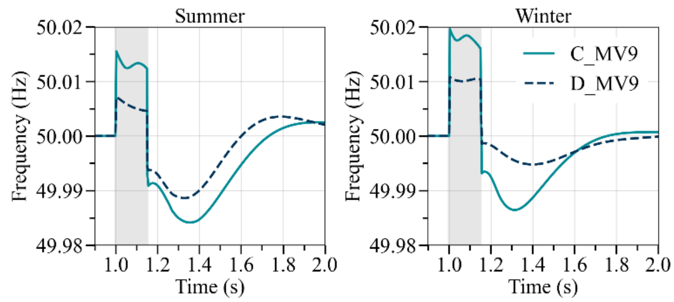

Figure 7. Frequency at MV9 during (grey) and after MV fault.

V. Discussion and Trade-Off Analysis

The vertical redistribution of IBRs fundamentally alters the dynamic behavior of multi-voltage level power systems. The results reveal that stability and resilience emerge from the interaction of frequency stiffness, voltage recovery, spatial fault containment, and converter coordination across the grid hierarchy. Fig. 8 synthesizes simulation results into a multi-dimensional performance comparison using the normalization methodology of Section III-C. Each radar chart axis aggregates related metrics across the observed ranges: frequency stability (nadir + RoCoF), voltage metrics (minima + recovery times), fault containment (spatial deviation), converter protection (tripping magnitude), and recovery speed (restoration times).

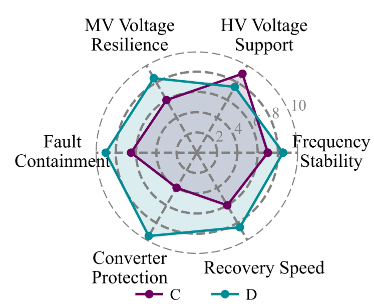

Figure 8. Comparison of C and D configurations across stability and resilience metrics.

Three key trade-offs emerge from this multi-dimensional comparison. First, frequency stiffness versus damping: concentrated configurations provide stronger instantaneous frequency support through aggregated inertial response, but this rigidity produces abrupt transients and persistent oscillations. Although total generation is unchanged, distributed layouts deliver higher effective early-time stiffness via fast active-power support and staggered tripping, cutting RoCoF by 30–50% and smoothing frequency trajectories.

Second, voltage support distribution: C concentrates reactive power at the HV level, yielding 8–23% higher voltage minima during HV faults, but creates vulnerability to cascading tripping (4:1 disconnection ratio). D distributes reactive reserves across voltage levels, accepting slightly lower HV nadirs in exchange for +0.03–0.07 p.u. MV voltage improvement, 37% faster recovery, and 76% fewer disconnections.

Third, centralized control versus spatial autonomy: C depends on inter-level coupling for power balance, making it susceptible to transformer congestion, line overload and delayed recovery. D enhances local autonomy through distributed BESS coordination, enabling rapid fault containment (deviations <0.01 Hz in neighboring areas) and 35–42% faster voltage recovery in Case 3.

Aggregated performance metrics quantify the trade-offs: across all cases and seasons, D improves voltage minima by +0.03–0.07 p.u., accelerates recovery by 0.2–0.3 s, and reduces total converter tripping by approximately 70%. These findings indicate that stronger electrical coupling does not necessarily improve stability in the examined inverter-dominated configurations. Instead, resilience depends on balanced allocation: sufficient HV capacity to maintain backbone integrity combined with adequate MV resources for localized support and containment. This suggests that future grid codes may benefit from considering not only total inverter capacity but also its vertical allocation across voltage levels to ensure both frequency stability and voltage resilience under diverse fault conditions.

VI. CONCLUSION AND OUTLOOK

This study demonstrates that the vertical distribution of IBRs across voltage levels strongly influences dynamic stability and operational resilience in the investigated low-inertia system. Simulations of three representative fault scenarios on a large-scale multi-voltage network revealed how redistributing generation capacity across voltage levels affects dynamic performance under different seasonal conditions.

Centralized (here high HV concentration) layouts provide stronger instantaneous frequency stiffness but experience deeper voltage fluctuations, higher converter tripping (up to 4:1 ratio in severe HV faults), and slower recovery. Distributed architectures yield smoother frequency damping, superior voltage resilience at MV level (+0.03–0.07 p.u.), faster recovery (0.2–0.3 s), and up to 70% lower tripping exposure. These results confirm that stability margins depend not only on converter control design but also on architectural decisions regarding capacity placement within the grid hierarchy.

Future work should integrate dynamic stability with time-series operational analysis to evaluate resilience over realistic annual cycles and to quantify improvement levers such as curtailment and transformer downsizing. It should also extend the framework with multi-criteria evaluation metrics and determine the minimum GFM share per voltage level required to sustain islanding and post-fault recovery. This integration enables a holistic understanding of how generation placement, degree of autonomy, and control hierarchy jointly shape the long-term stability and self-sufficiency of converter-dominated power systems.

ACKNOWLEDGMENT

This publication was developed as part of the research project SysZell (FKS 03EI4074A), funded by the German Federal Ministry for Economic Affairs and Climate Action. Only the authors are responsible for the content of this paper.

Supported by:

Federal Ministry for Economic Affairs and Climate Action

on the basis of a decision by the German Bundestag

REFERENCES

[1] IEA, "Renewables 2024 – Analysis and forecast to 2030," Paris, 2024. [Online]. Available: https://www.iea.org/reports/renewables-2024

[2] F. Milano, F. Dörfler, G. Hug, D. J. Hill, and G. Verbič, "Foundations and Challenges of Low-Inertia Systems (Invited Paper)," in *2018 Power Systems Computation Conference (PSCC)*, Dublin, Ireland, Jun. 2018 - Jun. 2018, pp. 1–25.

[3] J. Matevosyan *et al.,* "Grid-Forming Inverters: Are They the Key for High Renewable Penetration?," *IEEE Power and Energy Mag.*, vol. 17, no. 6, pp. 89–98, 2019, doi: 10.1109/MPE.2019.2933072.

[4] NERC, "1,200 MW Fault Induced Solar Photovoltaic Resource Interruption Disturbance Report, Southern California – August 16, 2016 Event," Jun. 2017. [Online]. Available: https://www.nerc.com/pa/rrm/ea/Documents/1200_MW_Fault_Induced_Solar_Photovoltaic_Resource_Interruption_Final.pdf

[5] R. H. Lasseter, "MicroGrids," in *2002 IEEE Power Engineering Society Winter Meeting. Conference Proceedings (Cat. No.02CH37309)*, New York, NY, USA, Jan. 2002, pp. 305–308.

[6] B. Uhlemeyer *et al.,* "Cellular approach as a principle in integrated energy system planning and operation," *CIRED - Open Access Proceedings Journal*, vol. 2020, no. 1, pp. 58–61, 2020, doi: 10.1049/oap-cired.2021.0021.

[7] M. Cabiati, C. Tornelli, and L. Martini, "The ELECTRA Web-of-Cells control architecture concept for the future power system operation," in *2018 AEIT International Annual Conference*, Bari, Italy, Oct. 2018 - Oct. 2018, pp. 1–6.

[8] M. Shabanzadeh, M.-K. Sheikh-El-Eslami, and M.-R. Haghifam, "The design of a risk-hedging tool for virtual power plants via robust optimization approach," *Applied Energy*, vol. 155, pp. 766–777, 2015, doi: 10.1016/j.apenergy.2015.06.059.

[9] G. Celli, E. Ghiani, S. Mocci, and F. Pilo, "A Multiobjective Evolutionary Algorithm for the Sizing and Siting of Distributed Generation," *IEEE Trans. Power Syst.*, vol. 20, no. 2, pp. 750–757, 2005, doi: 10.1109/TPWRS.2005.846219.

[10] A. Plietzsch, P. Schultz, J. Heitzig, and J. Kurths, "Local vs. global redundancy – trade-offs between resilience against cascading failures and frequency stability," *Eur. Phys. J. Spec. Top.*, vol. 225, no. 3, pp. 551–568, 2016, doi: 10.1140/epjst/e2015-50137-4.

[11] O. Smith, O. Cattell, E. Farcot, R. D. O'Dea, and K. I. Hopcraft, "The effect of renewable energy incorporation on power grid stability and resilience," *Sci. Adv.*, vol. 8, no. 9, 2022, doi: 10.1126/sciadv.abj6734.

[12] U. P. Müller *et al.,* "Integrated Techno-Economic Power System Planning of Transmission and Distribution Grids," *Energies*, vol. 12, no. 11, p. 2091, 2019, doi: 10.3390/en12112091.

[13] L. Pagnier and P. Jacquod, "Optimal Placement of Inertia and Primary Control: A Matrix Perturbation Theory Approach," *IEEE Access*, vol. 7, pp. 145889–145900, 2019, doi: 10.1109/ACCESS.2019.2945475.

[14] G. M. Tina, G. Maione, and D. Stefanelli, "The Impact of Grid-Forming vs. Grid-Following Converters on Frequency Regulation: Comparing Centralised or Distributed Photovoltaic Generation," *Energies*, vol. 17, no. 23, p. 5827, 2024, doi: 10.3390/en17235827.

[15] S. Meinecke *et al., SimBench Dokumentation: Elektrische Benchmarknetzmodelle*. Kassel: Universität Kassel, 2020.

[16] Orth, N., Weniger, J. & Meissner, L., "Empfehlungen zur Auslegung von Solarstromspeichern," 2022. [Online]. Available: https://solar.htw-berlin.de/publikationen/auslegung-von-solarstromspeichern/

[17] *PowerFactory*. Gomaringen, Deutschland.: DIgSILENT GmbH.

[18] ENTSO-E, *DYNAMIC MODEL OF CONTINENTAL EUROPE V2.* [Online]. Available: https://eepublicdownloads.blob.core.windows.net/public-cdn-container/clean-documents/SOC%20documents/CE_Dynamic_Model_v2_user_s_manual.pdf

[19] IEEE, "IEEE Application Guide for IEEE Std 1547-2018 IEEE Standard for Interconnection and Interoperability of Distributed Energy Resources with Associated Electric Power Systems Interfaces," 2020.

979-8-3315-8138-1